Hindawi
Science and Technology of Nuclear Installations
Volume 2023, Article ID 5897980, 10 pages
https://doi.org/10.1155/2023/5897980

Research Article

Analysis of the Effect of Applied Load on Crevice Corrosion Behavior

Fuqiang Yang,[1] **Yue Zhang**,[2] **and Jianzhou Zhang**[2]

[1]*Xi'an University of Science and Technology, School of Science, Xi'an 710054, China*
[2]*Xi'an University of Science and Technology, School of Mechanical Engineering, Xi'an 710054, China*

Correspondence should be addressed to Fuqiang Yang; yang_afreet@163.com

Received 29 September 2022; Revised 23 November 2022; Accepted 13 April 2023; Published 3 May 2023

Academic Editor: Kai Xu

A two-dimensional numerical model incorporating solid mechanics, electrochemistry, mass diffusion, and ion migration processes is developed to investigate the load effect on the crevice corrosion. The model is a transient model of crevice corrosion occurring in cracks of 304 stainless steel in a dilute NaCl solution, and the interaction between stress and electrochemical corrosion was considered. By solving the multiphysical coupling model in COMSOL, the effect of applied load on electrochemical corrosion in the crack tip region was calculated, and the local corrosion current density in the crack tip region with stress concentration within the crack was also calculated by using the Tafel relationship. The distribution of Fe^{2+} ion, Na^{+} ion, CL^{-} ion, and H and O_2 substance concentrations within the crack cavity is predicted by the equation analysis of substance transport. The results show that metal oxidation is more clearly affected by plastic deformation, the rate of hydrogen evolution reaction increases with stress enhancement, and the oxygen absorption reaction is not affected by stress strain. The distribution of iron ions, hydrogen, and oxygen within the crack is affected by the electrochemical reaction rate, and the distribution of iron ions, sodium ions, and chloride ions is affected by the electrolyte potential.

1. Introduction

Austenitic stainless steel 304 is widely used in the nuclear power industry for its excellent corrosion resistance and good machinability. It is mainly used to manufacture the key components in nuclear power plants such as the pressure vessel, core, in-vessel components, push rod, drive mechanism, circuit, piping and coolant pump, steam generator, heat exchanger, etc. [1] In the service process of these components, cracks and other defects could be inevitably induced by complex factors. When the crack length and width meet the conditions for the occurrence of crevice corrosion, corrosion media will enter into the crevice and result in crevice corrosion. Once crevice corrosion begins, the corrosion rate will rapidly increase and bring serious damage to the material and components [2].

It is reported that crevice corrosion could initiate due to the solution chemistry difference or electrode potential difference between the inside and outside of a crevice [3–5]. Kim et al. investigated the corrosion mass changes of canister candidate materials (Cu, Ni, Ti, and SS304) in an oxic groundwater solution. The results show that the Ni and Ti electrodes did not demonstrate any significant changes in the presence of chloride ions, whereas the SS304 electrode was slightly increased compared to the absence of chloride ions [6]. By establishing a mechanical submodel, the reaction transport submodel, and a crack repair submodel, Meng et al. quantitively investigated the interconnected influencing factors in practical engineering. The calculation results show that compared with electrolyte concentration, the influence of current density on crack closure rates are more obvious [7]. Meng et al. studied the localized corrosion of alloy 690 TT, and the results show that the scratch groove and the whole deformed region caused by scratching are considered as anode and correspond to the peak of tip current [8]. Unigovski et al. studied the corrosion creep of pure Mg and die-cast AZ91D alloy in borate and 3.5% NaCl solutions, and the results show that the effect of environment

on the creep behavior of magnesium is mainly connected with plasticization of metal assisted by chemical reactions [9]. The applied tensile stress, especially plastic stress, has a significant effect on the dissolution of steel [10–15].

In this paper, the effects of stress on crevice corrosion were studied by applying different displacement loads to the cracked stainless steel, and the local corrosion current density on the cracked surface was also calculated. By calculating the ion concentration distribution in the crack crevice, the influence of ions concentration on the stress as well as the electrolyte potential was analyzed.

2. Crack Crevice Corrosion Process

2.1. Chemical Equilibrium Reaction. When corrosion occurs, the main consideration is the anodic and cathodic reactions in the crack tip area; the crack wall is considered as a passivated surface that does not react. The main anodic reaction of the dissolution of the metal is described as (1), and the main cathodic reactions of the oxygen absorption reaction and the hydrogen evolution reaction are described as (2) and (3) separately [16]. The hydrogen evolution reaction is described as the single electron production of hydrogen atoms rather than the double electron production of hydrogen molecules. This is mainly because hydrogen atoms are dissolved in solution, and their penetration can embrittle the steel and endanger its structural integrity.

$$Fe \longrightarrow Fe^{2+} + 2e^{-}, \tag{1}$$

$$O_2 + 2H_2O + 4e^{-} \longrightarrow 4OH^{-}, \tag{2}$$

$$H^{+} + e^{-} \longrightarrow H. \tag{3}$$

The ion diffusion and electromigration occur during the crevice corrosion, so the solution in the crevice is considered static, and only Cl^{-}, Na^{+}, Fe^{2+}, O_2, and H will be considered in the mass transport process. As the length is much larger than the width of the crack crevice, the potential gradient and concentration gradient in the lateral direction can be considered zero, and only the electrochemical parameters in the direction of the length of the crevice and the change of ion concentration in the solution are considered. Moreover, the convection of ions is negligible due to the narrow crevice.

2.2. Electrochemical Kinetic Equations. During the occurrence of crevice corrosion, the potential of the electrolyte solution changes slowly and gradually reaches an equilibrium state; the ability to transport substances is related to the length of the crevice. According to Ohm's law and Laplace's equation, the potential in the crevice is controlled by

$$\frac{d^2E}{dx^2} = -\frac{i}{kw_2}, \tag{4}$$

where k is the conductivity of the electrolyte solution, $\mu S \cdot cm^{-1}$; w_2 is the width of the crevice, mm; and i is the current density in the crevice, $A \cdot m^{-2}$.

For crevice corrosion, the current density is caused by the oxidation of metals, the reduction of oxygen, and the hydrogen evolution [17] and can be described by the Tafel expression according to equations (5)~(8).

$$i_{\mathrm{Fe}} = i_{0,\mathrm{Fe}} \bullet 10^{\eta_{\mathrm{Fe}}/A_{\mathrm{Fe}}}, \tag{5}$$

$$i_{\mathrm{O}} = -\frac{C_{\mathrm{O}}}{C_{\mathrm{O,ref}}} \bullet i_{0,\mathrm{O}} \bullet 10^{\eta_{\mathrm{O}}/A_{\mathrm{O}}}, \tag{6}$$

$$i_{\mathrm{H}} = i_{0,\mathrm{H}} \bullet 10^{\eta_{\mathrm{H}}/A_{\mathrm{H}}}, \tag{7}$$

$$\eta = \varphi_s - \varphi_l - E_{\mathrm{eq}}, \tag{8}$$

where $i_{0,i}$ is the exchange current density of substance i, $A \cdot m^{-2}$; C_O is oxygen concentration, $mol \cdot m^{-3}$; $C_{O,ref}$ is initial oxygen concentration, $mol \cdot m^{-3}$; ηi is activated on overpotential of i, V; A_i is the Tafel slope for substance i, V; φ_s is the external potential, V; φ_l is the electrolyte potential, V; and E_{eq} is the equilibrium potential, V.

The additional chemical potential of atoms caused by dislocation in plastic metals will change the standard potential of metals [18] and could be expressed as equations (9)~(11):

$$\Delta E_{ae,eq} = -\frac{\Delta P V_m}{zF}, \tag{9}$$

$$\Delta E_{ap,eq} = -\frac{TR}{zF} \ln\left(\frac{\nu_{\mathrm{a}}\alpha}{N_0}\varepsilon_{\mathrm{p}} + 1\right), \tag{10}$$

$$E_{ap,eq} = E_{\mathrm{Fe},eq} - \frac{\Delta P V_{\mathrm{m}}}{zF} - \frac{TR}{zF} \ln\left(\frac{\nu_{\mathrm{a}}\alpha}{N_0}\varepsilon_{\mathrm{p}} + 1\right), \tag{11}$$

where $\Delta E_{ae,eq}$ and $\Delta E_{ap,eq}$ are the shifts of the equilibrium potential of an anodic reaction under elastic and plastic deformations, respectively, V; $E_{Fe,eq}$ is the equilibrium potential of iron under the condition of no elastic-plastic deformation, V; ΔP is the external excess pressure experienced by the metal, and it will be denoted with the absolute value of the hydrostatic part of the stress tensor, and equals to hydrostatic pressure in Comsol calculations, Pa; V_m is the mole volume of metal, m^3/mol; F is the Faraday's number, c/mol; T is the absolute temperature, K; R is the gas constant; z is the ion valence; ν_a is an orientation-dependent factor; α is a coefficient; and N_0 is the initial density of dislocations prior to plastic deformation, m^{-2}.

The exchange current density in the cathodic reaction subject to elastoplasticity is calculated by the following equations [19]:

$$i_{0,\mathrm{H}} = i_{0,\mathrm{H,ref}} \bullet 10^{\left(\sigma_{\mathrm{Mises}} \bullet V_{\mathrm{m}}/6F\left(-A_{\mathrm{H}}\right)\right)}, \tag{12}$$

$$i_{0,\mathrm{O}} = i_{0,\mathrm{O,ref}} \bullet 10^{\left(\sigma_{\mathrm{Mises}} \bullet V_{\mathrm{m}}/6F\left(-A_{\mathrm{O}}\right)\right)}, \tag{13}$$

where $i_{0,i,ref}$ is the exchange current density for substance i without external stress and strain, $A \cdot m^{-2}$; and σ_{Mises} is von Mises stress.

2.3. Dilute Matter Transport Equation in Electrolyte Solution. A mathematical model of the chemical and electrochemical environment in the crack crevice is established based on the mass transport equation of chemical substances in electrolyte solutions, which are considered diluted electrically neutral solutions. The transport of substances in electrolyte solutions is controlled by three mechanisms: diffusion, electromigration, and convection [20]. Considering the crack crevice is narrow, the convection in the crevice could be neglected, so the flux of the substance N_i in the solution is given by

$$N_{\mathrm{i}} = -z_{\mathrm{i}} F C_{\mathrm{i}} \frac{\partial \varphi}{\partial x} \frac{D_{\mathrm{i}}}{RT} - D_{\mathrm{i}} \frac{\partial C_{\mathrm{i}}}{\partial x}, \tag{14}$$

where N_i is fluxes of substances, mol·cm^{-2}·s^{-1}; u_i is the mobility of substance i, C_i is the concentration of substance i, mol·L^{-1}; φ is the potential, V; and D_i is the diffusion coefficient of substance i, cm^2·s^{-1}.

The transport of substance i along the crack crevice can be given by the following equations [21]:

$$R_{\mathrm{i}} = \frac{i_{\mathrm{net}}}{Z_{\mathrm{i}} F}, \tag{15}$$

$$\frac{\partial C_{\mathrm{i}}}{\partial t} = -\nabla N_{\mathrm{i}} + R_{\mathrm{i}}, \tag{16}$$

where R_i is the rate at which substance i is produced or consumed in a chemical reaction; i_{net} is the current density of the reaction; Z_i is the amount of charge transferred by substance i.

Substituting (14) and (15) into (16), the specific transport equation for substance i is obtained from following equation:

$$\frac{\partial C_{\mathrm{i}}}{\partial t} = \frac{z_{\mathrm{i}} F}{RT} D_{\mathrm{i}} \left(\frac{\partial C_{\mathrm{i}}}{\partial x} \frac{\partial \varphi}{\partial x} + C_{\mathrm{i}} \frac{\partial^2 \varphi}{\partial x^2} \right) + D_{\mathrm{i}} \frac{\partial^2 C_{\mathrm{i}}}{\partial x^2} + \frac{i_{\mathrm{net}}}{Z_{\mathrm{i}} F}. \tag{17}$$

3. FEM Simulations

3.1. Material. The PLD-50 fatigue tensile tester was used to perform uniaxial tensile tests on plate tensile specimens of 304 austenitic stainless steel with a standard distance segment of 20 mm to obtain their uniaxial tensile mechanical properties. The experiments were conducted at room temperature, and the specimens werestretched to fracture at a speed of 2 mm/min. The obtained engineering stress-strain curve was converted using the formula to obtain the real stress-strain curve, as shown in Figure 1, and the obtained real stress-strain curve was simulated by adding the hardening function to the plastic deformation behavior in the model to ensure the accuracy of the simulation calculation.

Electrochemical parameters are mainly from reference [19], and other parameters are from reference [22–25], The main parameters to be used during the simulation are listed in Tables 1 and 2:

3.2. Geometric Models and Mesh. According to the geometric symmetry of the crack gap and the homogeneity of the solution, the shape of the specimen is simplified as a rectangle with a length of $2W$ and a width of W, with a crack of depth L_1 and width L_2 on the left side of the specimen, and the crack tip is an arc with a radius equal to r. The half-simplified model of the specimen is shown in Figure 2(a), where region 1 is the crack crevice filled by NaCl solution, region 2 is the metal, and R_1 and R_2 are defined as analysis paths. The overall free triangle mesh is used to divide the model, and the mesh is refined in the crack tip region to achieve high solution accuracy, as shown in Figures 2(b) and 2(c).

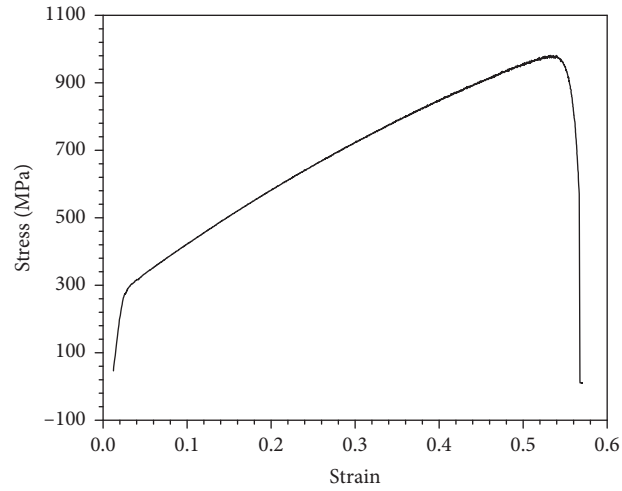

Figure 1: Real stress-strain curve of austenitic stainless steel 304.

Table 1: Geometrical and electrochemical parameters.

Parameters	Values
Crack depth L_1 (mm)	5
Crack width L_2 (mm)	0.1
Faraday's number F (C·mol^{-1})	96500
External potential φ_s (V)	−0.4
Electrical conductivity k (μS·cm^{-1})	9400
Tafel slope of hydrogen A_{H} (V)	−0.15
Tafel slope of oxygen A_{O2} (V)	−0.18
Initial oxygen concentration $C_{\mathrm{O2,ref}}$ (mol·L^{-1})	2.29×10^{-4}
Standard potential of hydrogen $E_{\mathrm{eq\text{-}H}}$ (V)	−1.03
Standard potential of oxygen $E_{\mathrm{eq\text{-}O2}}$ (V)	0.189
Standard potential of iron $E_{\mathrm{eq\text{-}Fe}}$ (V)	−0.76
Exchange current density of hydrogen $i_{0,\mathrm{H}}$ (A·m^{-2})	1.1×10^{-2}
Exchange current density of oxygen $i_{0,\mathrm{O2}}$ (A·m^{-2})	7.7×10^{-7}
Diffusion coefficient of iron ion $D_{\mathrm{Fe2+}}$ (cm^2·s^{-1})	7.2×10^{-6}
Diffusion coefficient of sodium ion $D_{\mathrm{Na+}}$ (cm^2·s^{-1})	1.334×10^{-5}
Diffusion coefficient of chloride ion $D_{\mathrm{Cl-}}$ (cm^2·s^{-1})	2.032×10^{-5}
Diffusion coefficient of oxygen D_{O2} (cm^2·s^{-1})	2.29×10^{-5}
Diffusion coefficient of hydrogen D_{H} (cm^2·s^{-1})	3.3×10^{-5}
Solution concentration C_{NaCl} (mol·L^{-1})	0.01

3.3. Initial Value and Boundary Conditions. To achieve the assumption of fast reaction kinetics, an external potential φ_s on the anode surface at the crack tip of the model was set to a constant potential; the equilibrium potential was set to a constant value; and the main condition of the electrode reaction was set to thermodynamic equilibrium. The slit wall

Table 2: Material parameters and constant.

Parameters	Values
Elastic modulus E (Pa)	1.76×10^{11}
Poisson's ratio ν_{p_3}	0.3
Density ρ (kg/m^3)	7930
Yield stress (Pa)	3.09×10^8
Mole volume of metal V_m (m^3·mol^{-1})	7.13×10^{-6}
Absolute temperature T (K)	298.15
Gas constant R (J·(mol·K)$^{-1}$)	8.314
Coefficient ν_a	0.45
Initial density of dislocations prior N_0 (m^{-2})	1.67×10^{15}

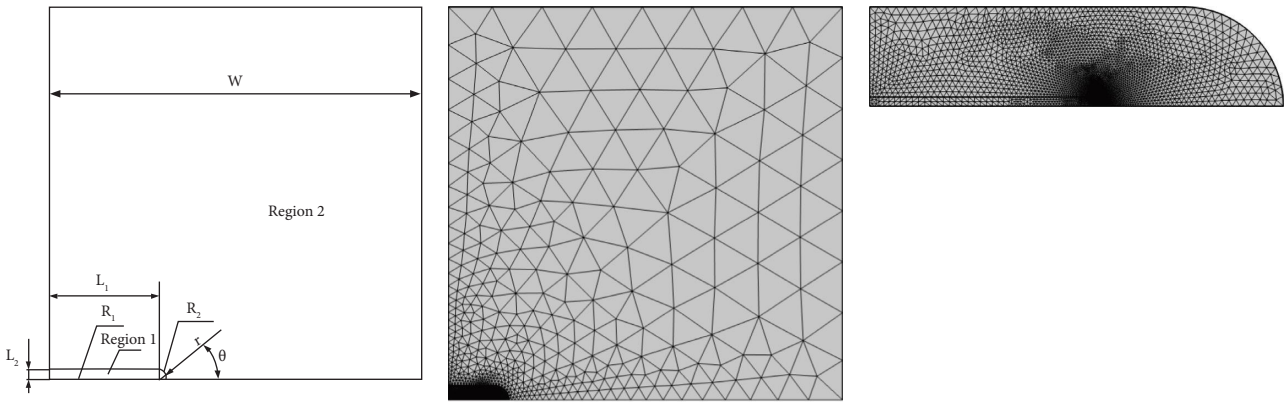

Figure 2: Geometry and meshing, (a) geometry, (b) overall meshing, and (c) cracked area meshing.

and the crack tip were considered a passivated surface and an electrode surface with activity separately. To exclude other factors from influencing the crack tip and slit wall, it is assumed that the boundary flux is zero and no hydrogen flows in and out of the model boundary location. The concentration of the electrolyte solution at the initial moment in the crack crevice is 0.01 mol/L sodium chloride solution; the initial pH of the electrolyte solution is 6.8; according to the Faraday's law, the oxygen reduction reaction will produce oxygen flux at the crack crevice opening and to ensure the authenticity of the simulation results, the oxygen concentration content in the atmospheric concentration is used as the initial value of the oxygen concentration variable. Different displacement loads are applied to the upper boundary of the model.

4. Results and Discussion

4.1. Corrosion of Cracked Surfaces. For a clearer and more precise analysis of electrochemistry affected by stress-strain, the case without applied load was added to the calculation, when the metal does not produce any elastic-plastic change and the corrosion inside the crack is not affected by the load, and the results of this calculation were set as a control group.

Figure 3(a) shows the Mises stresses generated on the crack profile with different applied displacement loads. The stress has maximum value at a crack tip ($\theta = 0^\circ$) and decreases gradually along the crack contour on both sides. When the applied displacement load $d = 0.05$ mm, there is no stress change in the crack profile from 0° to 59°, and the stress is 355.3 MPa. When $d = 0.08$ mm, the stress change from 22° to 66° is smaller and the same at 355.3 MPa. The stresses in all other cases of displacement load are gradually increasing. Figure 3(b) shows the equivalent plastic strain at the crack contour. It can be seen that, at $d = 0.02$ mm, the stress is small compared to the yield stress, and no significant plastic strain occurs, while the other three loads produce large plastic.

Figure 4(a) shows the local corrosion current density distribution of the hydrogen evolution reaction on the surface of the crack contour, which reflects the corrosion velocity. When the applied load is 0, the local current corrosion keeps consistent around the crack tip contour; when the specified load displacement d increases to 0.02 mm, even though the crack tip has only elastic deformation and no plastic deformation, according to Figure 3, the corrosion current of hydrogen evolution reaction still has a large change compared to the initial condition of no applied load, and its growth trend is similar to the distribution of von Mises stress, which indicates that the increase in corrosion current density is mainly affected by stress. When the applied load d increased to 0.11 mm, the current density is significantly enhanced by the stress and has a peak of -0.1 A/m^2 at the crack tip. The results show that the corrosion strength increases with increasing stress.

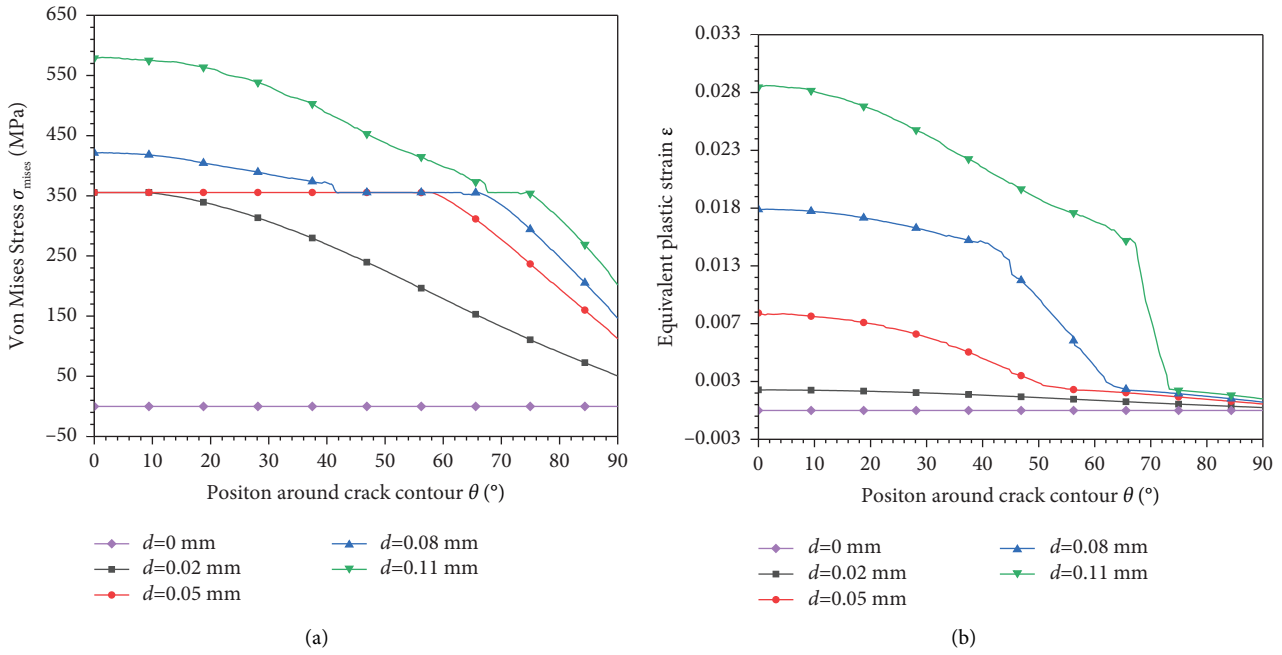

FIGURE 3: Stress and strain around the crack contour under different applied displacement loads. (a) Von Mises stress. (b) Equivalent plastic strain.

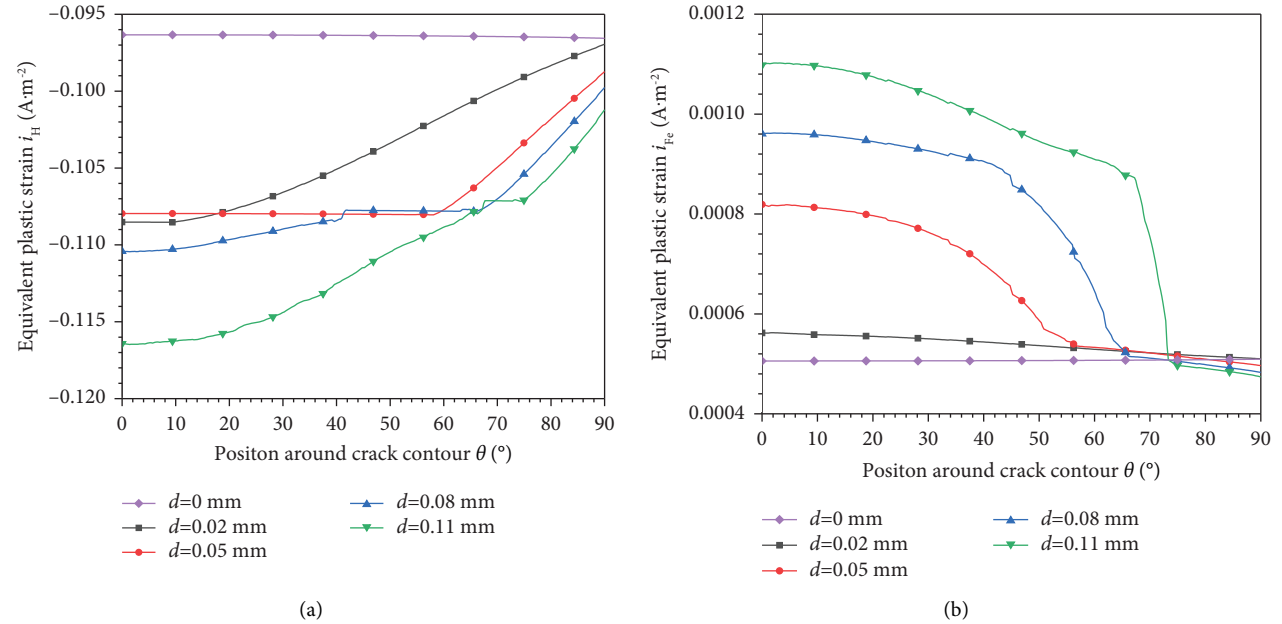

FIGURE 4: Continued.

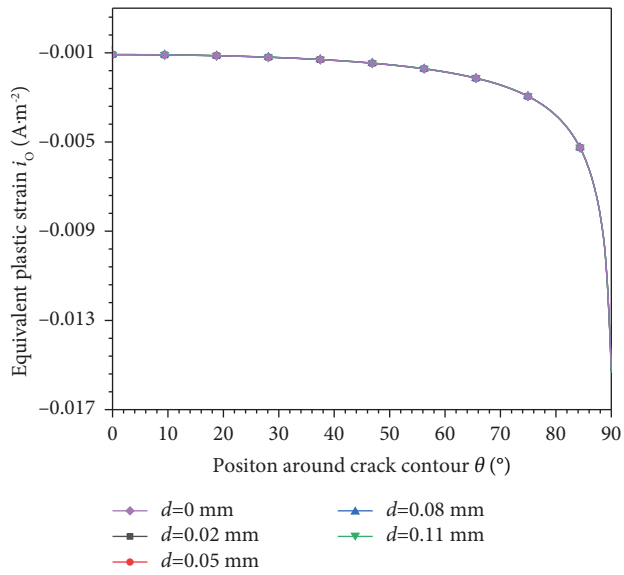

(c)

FIGURE 4: Local corrosion current density around the crack contour under different applied displacement loads; (a) hydrogen evolution reaction; (b) iron oxidation reaction; and (c) oxygen absorption reaction.

Figure 4(b) shows the distribution of the local corrosion current density over the crack contour for the iron oxidation reaction. When the boundary designation displacement is 0.02 mm, the increase of corrosion current density is not obvious compared to initial condition, but the corrosion current density increased dramatically when the load increased to 0.05 mm, 0.08 mm, and 0.11 mm. By comparing Figure 3, it can be seen that when the load displacement is 0.02 mm, the equivalent plastic deformation produced is small, even though there is also an obvious stress concentration on the crack tip. In the case of the other three applied displacement loads, the plastic deformation is large, so it is indicated that anodic galvanic corrosion is mainly influenced by plastic deformation. The larger the boundary displacement load, the stronger the corrosion current on the surface of the crack. As the crack tip has the maximum plastic deformation, the corrosion current density is much enhanced here and decreased with increased angle along the crack contour. When $d = 0.11$ mm, a larger equivalent plastic strain is generated, i_{Fe} is significantly enhanced by 137.49% around 0°–73° than the other regions.

Figure 4(c) shows the distribution of the local corrosion current density of oxygen absorption reaction on the crack contour. The calculation results show that the local current density of oxygen absorption corrosion seems unchanged under different loads. Even though the increased load displacement increased the oxygen absorption and corrosion velocity, the oxygen consumption increased correspondingly. Due to the low level of dissolved oxygen inside the crack, the consumed oxygen at the crack tip could only be supplied by the diffusion of oxygen via the small crack opening crevice. However, the supply of oxygen could not meet the increased oxygen absorption velocity, so the oxygen absorption reaction seems to be the same with different load conditions, and the reaction is controlled by the diffusion of oxygen diffusion in the crevice.

4.2. Mass Transports in the Crack Crevice. Figure 5 shows the concentration distribution of Fe^{2+} in the crevice under different load condition. According to (17), the distribution of Fe^{2+} is affected by the dissolved metal, its diffusion under a concentration gradient, and the electrolyte potential. As metal Fe dissolve as Fe^{2+} at the crack tip, the concentration of Fe^{2+} is the highest at the crack tip, which leads to the concentration gradient and drives the Fe^{2+} diffusion along the crevice to the crack mouth, thus a gradually decreased concentration towards the crack mouth. However, the concentration differences around the crack contour are very small due to the tiny crack tip. With the increase of the load displacement, the concentration of Fe^{2+} increases along the crevice, and that is because the dissolve velocity of metal increases with the load displacement.

Figure 6 shows the change of electrolyte potential under different load conditions. The larger the external load, the lower the electrolyte potential at the crack tip, which blocks the Fe^{2+} diffusion towards the crack mouth; however, the effects of electrolyte potential between both ends to block the diffusion are smaller than the driving force caused by the concentration gradient. The combined effects of potential and concentration gradient lead to the Fe^{2+} distribution as shown in Figure 6(a).

Figure 7 shows the distribution of hydrogen concentration in the crevice under different loads. As the local corrosion current density increases with the increase in load, the hydrogen generation velocity at the crack tip also increases with the increased load, and the hydrogen concentration decreases towards the crack mouth, as shown in Figure 7. Since the hydrogen is electrically neutral, its

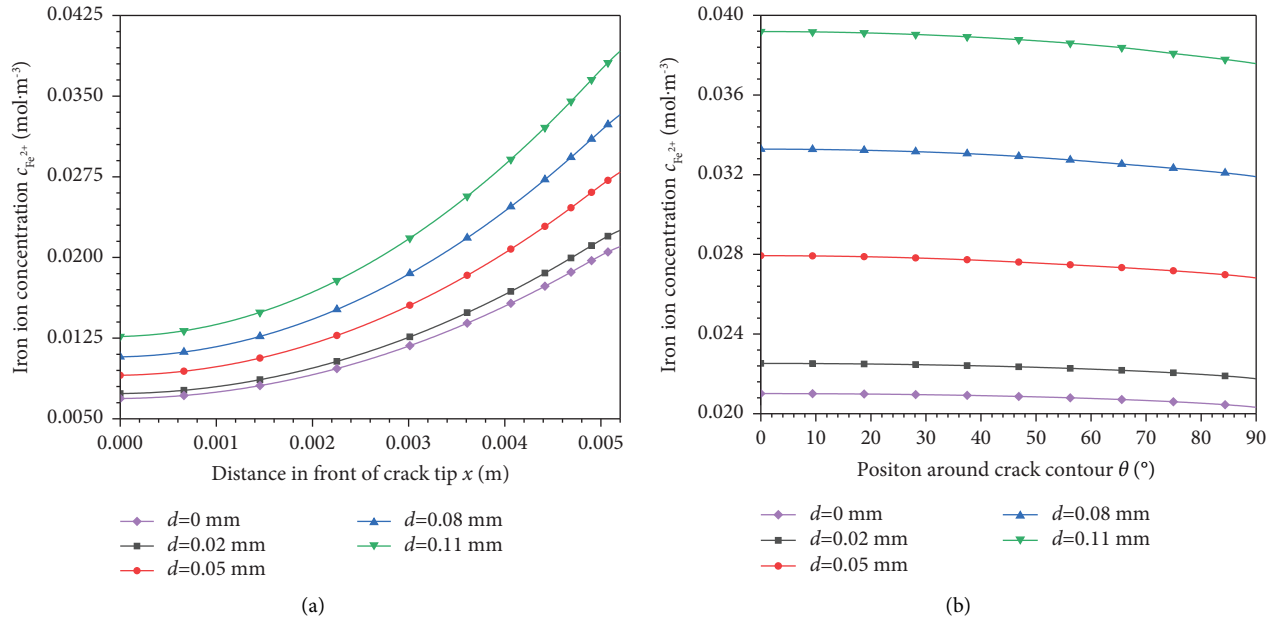

FIGURE 5: Fe^{2+} concentration in the crack under different applied displacement loads (a) on path R_1 and (b) on path R_2.

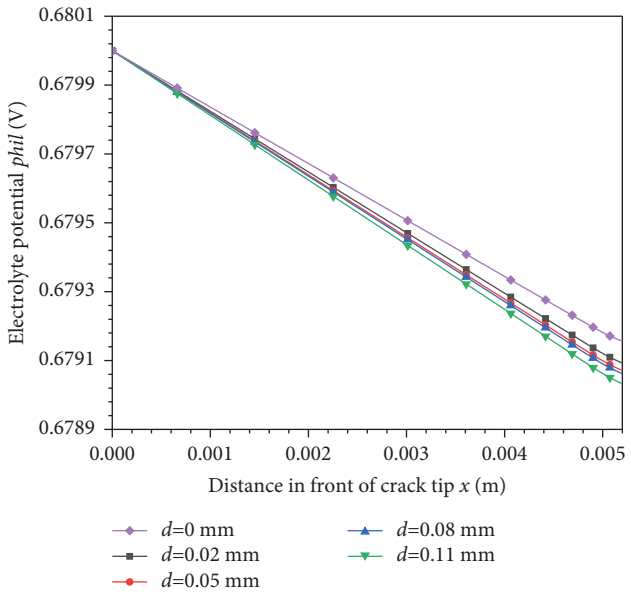

FIGURE 6: Electrolyte potential in the crack under different applied displacement loads.

distribution within the crevice is mainly influenced by electrochemical corrosion as well as the diffusion of the substance. Compared with Fe^{2+}, hydrogen has a higher diffusion coefficient and is not affected by the electrolyte potential, and its diffusion to the crevice mouth is faster.

Figure 8 shows the oxygen concentration distribution in the crevice under different loads, and the distribution is only influenced by the concentration gradient and electrochemical corrosion rate. The oxygen on the crack surface is consumed rapidly, and the oxygen on the crack mouth diffuses freely towards the crack tip, which leads to a gradual decrease of oxygen concentration towards the crack tip, as shown in Figures 8(a) and 8(b), the oxygen concentration along the crack contour has the minimum value at the crack tip and increases towards the crack wall, which indicates a faster oxygen consumption at the crack tip than on both sides. However, the oxygen concentration near the crack tip is so small that the corrosion current densities have little difference with different applied loads, so there is no significant difference in the oxygen distribution in the crevice.

Figure 9 shows the concentration distribution of Na^+ and Cl^- within the crevice, which is only affected by the concentration gradient and electrolyte potential. Since the electrolyte potential decreases from the crack mouth to the

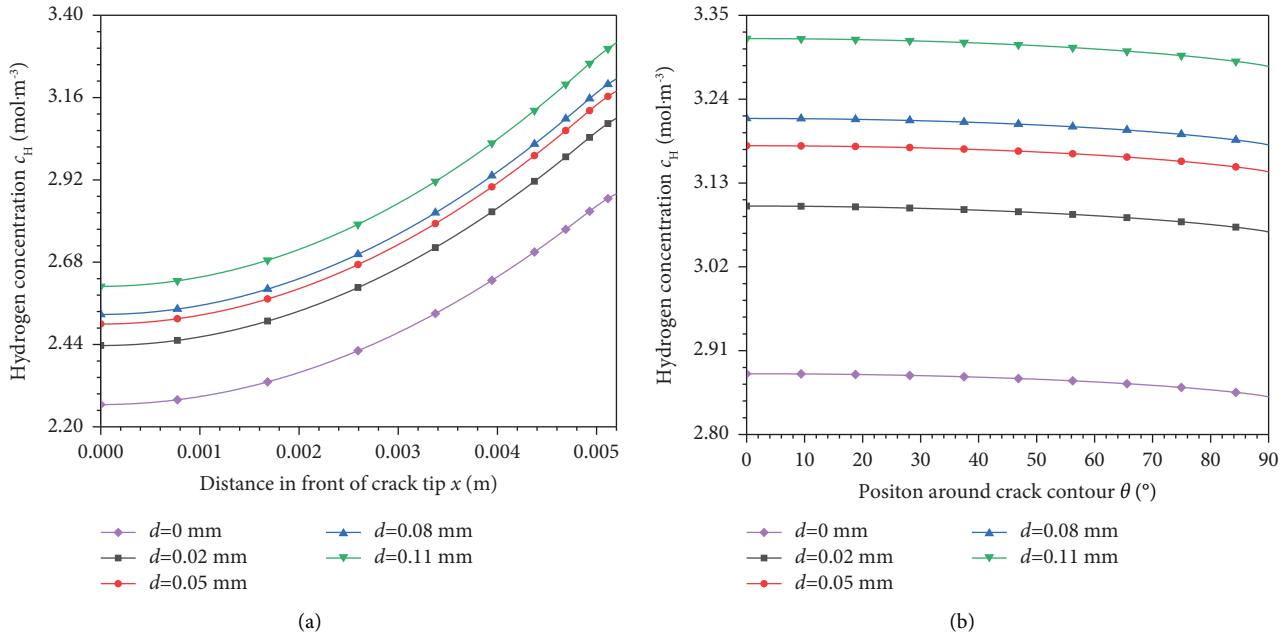

FIGURE 7: Hydrogen concentration in the crack under different applied displacement loads (a) on path R_1 and (b) on path R_2.

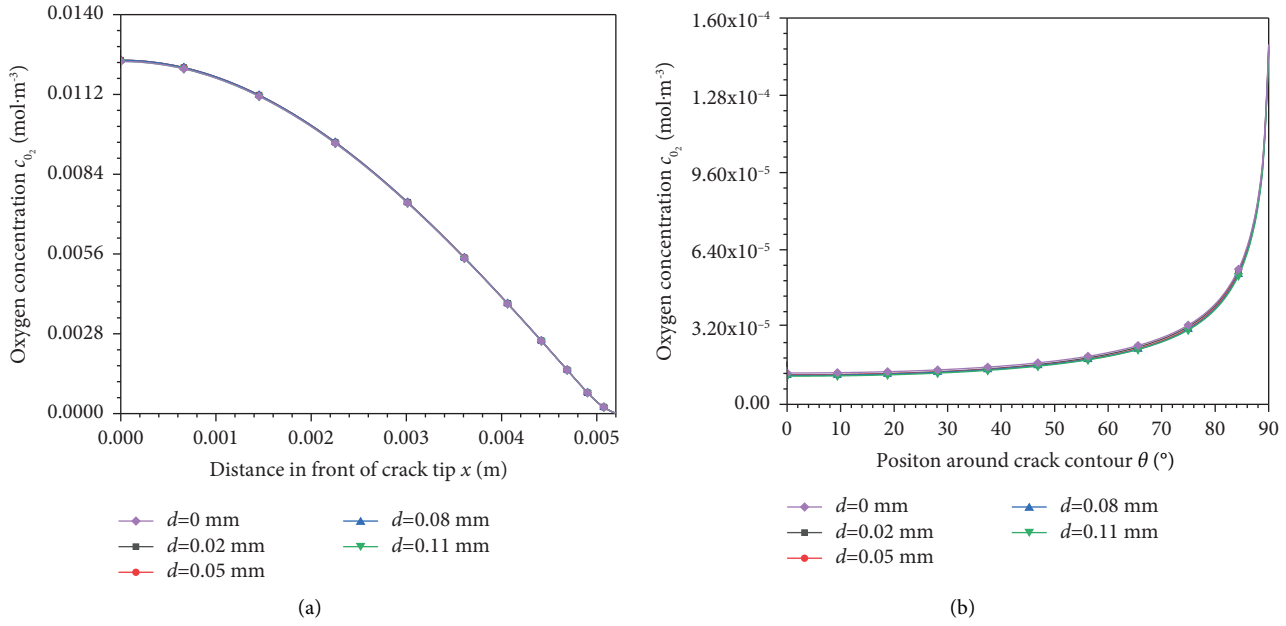

FIGURE 8: Oxygen concentration in the crack under different applied displacement loads: (a) on path R_1 and (b) on path R_2.

crack tip and their differences with the increase in applied load, Na^+ with a positive charge will migrate towards the inside of the crevice, and Cl^- with a negative charge will migrate towards the crack mouth. Thus, a gradual increase of Na^+ and a gradual decrease of Cl^- along the crevice towards the crack tip could be found. And with increased load displacement, the concentration differences at both ends increase.

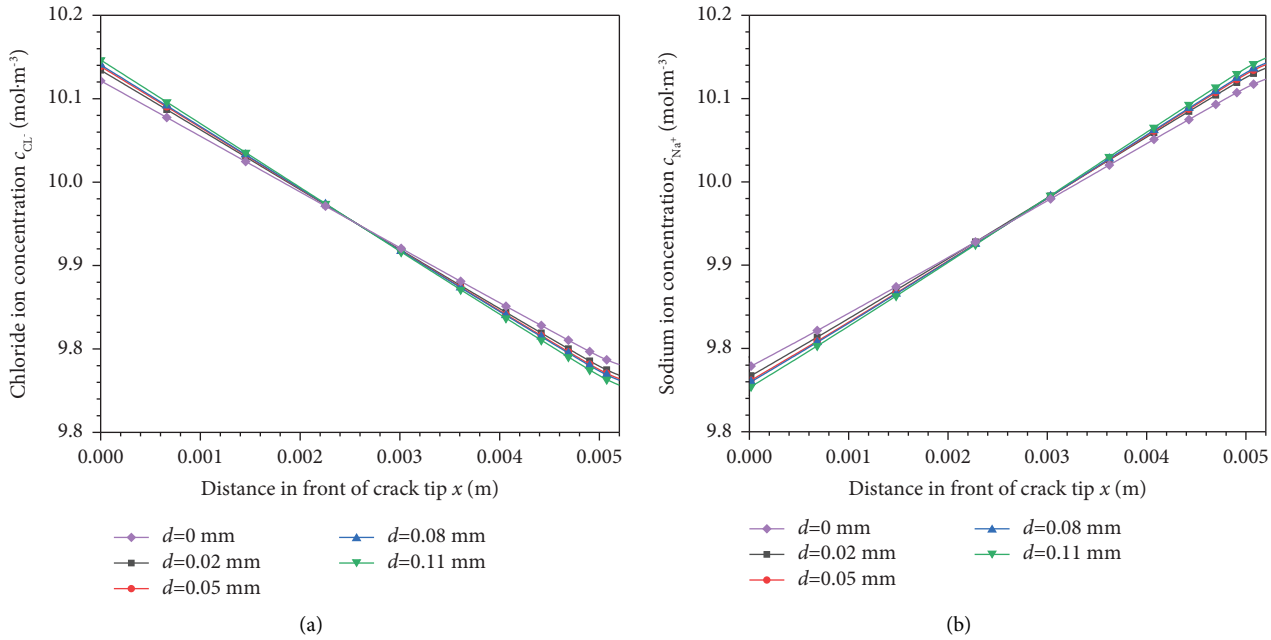

FIGURE 9: Concentration in the crack inner path R_1 under different applied displacement loads (a) Cl^- and (b) Na^+.

5. Conclusions

(1) When the electrochemical reaction occurs within the crack, the iron oxidation reaction in the anode is mainly affected by plastic deformation, and the corrosion rate accelerates with the increase of the equivalent plastic strain. Within the electrolyte, Fe dissolves into Fe^{2+} at the crack tip and then diffuses to the crack mouth. The diffusion process of Fe^{2+} is resisted by electrolyte potential. The dissolution velocity of Fe increases with increased load.

(2) The hydrogen evolution reaction velocity increases with the increase in applied load and leads to a gradual decrease in concentration trend towards crack mouth.

(3) Due to the low dissolved oxygen, the oxygen absorption reaction at the crack tip is not affected by the load condition and it is controlled by the oxygen diffusion in the crevice. The oxygen concentration decreases towards the crack tip.

(4) Influenced by the electrolyte potential, Cl^- migrates towards the crack mouth and Na^+ migrates towards the crack tip.

Data Availability

The data used to support the findings of this study were calculated according to the finite element method, and they are included in the article. The parameters used in the calculation model were cited from the references listed.

Conflicts of Interest

The authors declare that there are no conflicts of interest regarding the publication of this paper.

Acknowledgments

This work was supported by the National Natural Science Foundation of China (Grant no. 52175145) and the Key Research and Development Program of Shaanxi (Program no. 2023-YBGY-112).

References

[1] B. Li, *The Microstructure and Stress CorrosionCracking Behavior Study of Nuclear Plant304 Stainless Steel Welded Joints*, Tianjin University, China, 2016.

[2] D. X. Chen, X. Q. Wu, and E. H. Han, "Research progress of crevice corrosion and crevice corrosion lssues of nuclear-grade materials," *Journal of Chinese Society for Corrosion and Protection*, vol. 34, no. 04, pp. 295–300, 2014.

[3] M. I. Abdulsalam, "The role of electrolyte concentration on crevice corrosion of pure nickel," *Materials and Corrosion*, vol. 58, no. 7, pp. 511–513, 2007.

[4] R. M. Carranza and M. A. Rodríguez, "Crevice corrosion of nickel-based alloys considered as engineering barriers of geological repositories," *Npj Materials Degradation*, vol. 1, no. 1, 2017.

[5] Y. Z. Li, N. Xu, G. R. Liu, X. Guo, and G. Zhang, "Crevice corrosion of N80 carbon steel in CO2-saturated environment containing acetic acid," *Corrosion Science*, vol. 112, pp. 426–437, 2016.

[6] G. Y. Kim, S. W. Kim, J. Jang, S. Yoon, and J. S. Kim, "Investigation of early corrosion behavior of canister candidate materials in oxic groundwater by the EQCM method," *Science and Technology of Nuclear Installations*, vol. 2022, Article ID 4582625, 6 pages, 2022.

[7] Z. Meng, Q. Liu, J. Xia et al., "Mechanical–transport–chemical Modeling of Electrochemical Repair Methods for Corrosion-induced Cracking in marine concrete," *Computer-Aided Civil and Infrastructure Engineering*, vol. 37, 2022.

[8] F. J. Meng, E. H. Han, J. Q. Wang, Z. Zhang, and W. Ke, "Localized corrosion behavior of scratches on nickel-base Alloy 690TT," *Electrochimica Acta*, vol. 56, no. 4, pp. 1781–1785, 2011.

[9] Y. Unigovski, Z. Keren, A. Eliezer, and E. Gutman, "Creep behavior of pure magnesium and Mg–Al alloys in active environments," *Materials Science and Engineering: A*, vol. 398, no. 1-2, pp. 188–197, 2005.

[10] Z. Wang, F. Xie, D. Wang, and J. Liu, "Effect of applied potential on stress corrosion cracking behavior of X80 steel in alkaline soil simulated solution with sulfate-reducing bacteria," *Engineering Failure Analysis*, vol. 121, Article ID 105109, 2021.

[11] B. T. Lu, J. L. Luo, P. R. Norton, and H. Ma, "Effects of dissolved hydrogen and elastic and plastic deformation on active dissolution of pipeline steel in anaerobic groundwater of near-neutral pH," *Acta Materialia*, vol. 57, no. 1, pp. 41–49, 2009.

[12] Z. Li, X. Xu, Y. Li, and Z. Liu, "Effect of imidazoline inhibitor on stress corrosion cracking of P110 steel in simulated annulus environments of CO_2 injection well," *Journal of Electroanalytical Chemistry*, vol. 886, Article ID 115105, 2021.

[13] Y. H. Huang, F. Z. Xuan, S. T. Tu, and T. Itoh, "Effects of hydrogen and surface dislocation on active dissolution of deformed 304 austenitic stainless steel in acid chloride solution," *Materials Science and Engineering: A*, vol. 528, no. 3, pp. 1882–1888, 2011.

[14] E. M. Gutman, "An inconsistency in "film rupture model" of stress corrosion cracking," *Corrosion Science*, vol. 49, no. 5, pp. 2289–2302, 2007.

[15] M. Sahal, J. Creus, R. Sabot, and X. Feaugas, "Consequences of plastic strain on the dissolution process of polycrystalline nickel in H_2SO_4 solution," *Scripta Materialia*, vol. 51, no. 9, pp. 869–873, 2004.

[16] X. Chen, F. Gao, Y. Wang, and C. He, "Transient numerical model for crevice corrosion of pipelines under disbonded coating with cathodic protection," *Materials and Design*, vol. 89, pp. 196–204, 2016.

[17] W. Wang, K. Shen, J. Yi, and Q. Wang, "A mathematical model of crevice corrosion for buried pipeline with disbonded coatings under cathodic protection," *Journal of Loss Prevention in the Process Industries*, vol. 41, pp. 270–281, 2016.

[18] F. Yang, H. Xue, L. Zhao, and X. Fang, "Effects of stress intensity factor on electrochemical corrosion potential at crack tip of nickel-based alloys in high temperature water environments," *Rare Metal Materials and Engineering*, vol. 43, no. 3, pp. 513–518, 2014.

[19] L. Y. Xu and Y. F. Cheng, "Development of a finite element model for simulation and prediction of mechanoelectrochemical effect of pipeline corrosion," *Corrosion Science*, vol. 73, pp. 150–160, 2013.

[20] E. H. Han, J. M. Chen, and Y. J. Su, "Corrosion protection techniques of marine engineering structure and ship equipment——current status and future trend," *Materials China*, vol. 33, no. 2, pp. 65–76, 2014.

[21] J. Newman and K. E. Thomas-Alyea, *Electrochemical systems*, John Wiley and Sons, New Jersey, USA, 2012.

[22] S. M. Sharland and P. W. Tasker, "A mathematical model of crevice and pitting corrosion—I. The physical model," *Corrosion Science*, vol. 28, no. 6, pp. 603–620, 1988.

[23] A. Rao, J. Maclay, and S. Samuelsen, "Efficiency of electrochemical systems," *Journal of Power Sources*, vol. 134, no. 2, pp. 181–184, 2004.

[24] K. Yaya, Y. Khelfaoui, B. Malki, and M. Kerkar, "Numerical simulations study of the localized corrosion resistance of AISI 316L stainless steel and pure titanium in a simulated body fluid environment," *Corrosion Science*, vol. 53, no. 10, pp. 3309–3314, 2011.

[25] E. B. Muehlenkamp, M. D. Koretsky, and J. C. Westall, "Effect of moisture on the spatial uniformity of cathodic protection of steel in reinforced concrete," *Corrosion*, vol. 61, no. 6, pp. 519–533, 2005.